

Crystal Structure of $\text{Na}_2\text{V}_2(\text{PO}_4)_3$, an Intriguing Phase Spotted in the $\text{Na}_3\text{V}_2(\text{PO}_4)_3-\text{Na}_1\text{V}_2(\text{PO}_4)_3$ System

Sunkyu Park, Ziliang Wang, Zeyu Deng, Iona Moog, Pieremanuele Canepa,* François Fauth, Dany Carlier, Laurence Croguennec, Christian Masquelier, and Jean-Noël Chotard*



Cite This: <https://doi.org/10.1021/acs.chemmater.1c04033>



Read Online

ACCESS |

Metrics & More

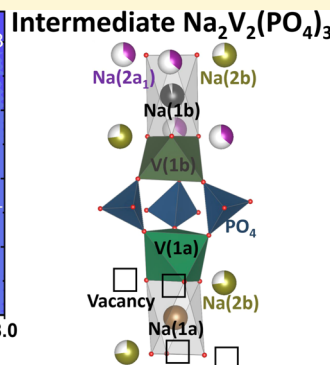
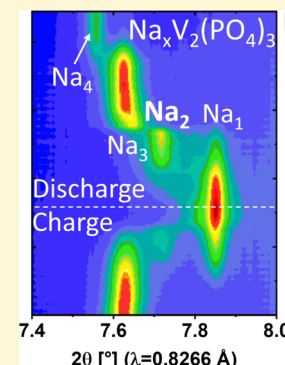
Article Recommendations

Supporting Information

ABSTRACT: The Na superionic conductor (NASICON) $\text{Na}_3\text{V}_2(\text{PO}_4)_3$ is an important positive electrode material for Na-ion batteries. Here, we investigate the mechanisms of phase transition in $\text{Na}_x\text{V}_2(\text{PO}_4)_3$ ($1 \leq x \leq 4$) upon nonequilibrium battery cycling. Unlike the widely believed two-phase reaction in a $\text{Na}_3\text{V}_2(\text{PO}_4)_3-\text{Na}_1\text{V}_2(\text{PO}_4)_3$ system, we determine, for the first time, the structure of a recently reported intermediate $\text{Na}_2\text{V}_2(\text{PO}_4)_3$ phase using operando synchrotron X-ray diffraction. Density functional theory calculations further support the existence of the $\text{Na}_2\text{V}_2(\text{PO}_4)_3$ phase. We propose two possible crystal structures of $\text{Na}_2\text{V}_2(\text{PO}_4)_3$ analyzed by Rietveld refinement. The two structure models with the space groups $P2_1/c$ or $P2/c$ for the new intermediate $\text{Na}_2\text{V}_2(\text{PO}_4)_3$ phase show similar unit cell parameters but different atomic arrangements, including vanadium charge ordering. As the appearance of the intermediate $\text{Na}_2\text{V}_2(\text{PO}_4)_3$ phase is accompanied by symmetry reduction, Na(1) and Na(2) sites split into several positions in $\text{Na}_2\text{V}_2(\text{PO}_4)_3$, in which one of the splitting Na(2) position is found to be a vacancy, whereas the Na(1) positions are almost fully filled. The intermediate $\text{Na}_2\text{V}_2(\text{PO}_4)_3$ phase reduces the lattice mismatch between $\text{Na}_3\text{V}_2(\text{PO}_4)_3$ and $\text{Na}_1\text{V}_2(\text{PO}_4)_3$ phases, facilitating a fast phase transition. This work paves the way for a better understanding of great rate capabilities of $\text{Na}_3\text{V}_2(\text{PO}_4)_3$.

INTRODUCTION

Na superionic conductor (NASICON)-structured materials are considered as promising electrodes for sodium-ion batteries because of their 3D open-framework crystal structure, resulting in high cyclability and fast rate capability.^{1–5} Among them, $\text{Na}_3\text{V}_2(\text{PO}_4)_3$ has been extensively studied, showing satisfactory energy density and rate performance as well as good thermal stability.^{6–13} The crystal structure of $\text{Na}_3\text{V}_2(\text{PO}_4)_3$ is composed of repeating units called lanterns, into which two VO_6 octahedra are joined together through three corner-sharing PO_4 tetrahedra. Within the 3D framework generated by these lanterns, two crystallographic sodium sites, labeled Na(1) and Na(2), are usually reported. The Na(1) site is located between the lantern units along the [001]_{hexagonal} direction and is surrounded by six oxygen atoms in its first coordination sphere and by six Na(2) atoms in its second one. At maximum, the Na(1) and Na(2) sites (of different multiplicities) can, respectively, generate one and three Na positions per formula unit, thus leading to the final stoichiometry $\text{Na}_4\text{V}_2(\text{PO}_4)_3$. During electrochemical reactions, although the Na(1) site is involved in the global Na-ion transport mechanism [Na(2)–Na(1)–Na(2) pathways], it tends to be almost fully occupied regardless of the total Na



content into the material, whereas the Na(2) site is partially/fully emptied or filled depending on the compositions.^{8,9,14–16}

It is well-known that two Na^+ ions can be reversibly electrochemically extracted from a $\text{Na}_3\text{V}_2(\text{PO}_4)_3$ electrode, through a voltage-composition “plateau” at ~ 3.4 V (vs Na^+/Na) utilizing the $\text{V}^{4+/3+}$ redox couple (with a theoretical capacity of 117.6 mA h/g).^{13,17–22} The reaction has been described by many authors as a mechanism of a two-phase reaction between $\text{Na}_3\text{V}_2^{3+}(\text{PO}_4)_3$ and $\text{Na}_1\text{V}_2^{4+}(\text{PO}_4)_3$.^{13,17–22} Additionally, one Na^+ ion can be inserted into $\text{Na}_3\text{V}_2(\text{PO}_4)_3$ at ~ 1.6 V (vs Na^+/Na) through the $\text{V}^{3+/2+}$ redox couple toward the $\text{Na}_4\text{V}_2(\text{PO}_4)_3$ composition (theoretical capacity of 58.8 mA h/g).^{18,19,22–27} Recently, Zakharkin et al.²⁰ noticed the signature of an intermediate $\text{Na}_2\text{V}_2(\text{PO}_4)_3$ phase, which involves the $\text{V}^{4+/3+}$ redox couple. Nevertheless, no structural information on the intermediate phase was provided. Other previous reports also suggested the existence of $\text{Na}_2\text{V}_2(\text{PO}_4)_3$,

Received: November 22, 2021

Revised: December 10, 2021

but the authors barely contemplated the existence of a new intermediate phase.^{18,19} This suggests that the widely believed two-phase reaction between $\text{Na}_3\text{V}_2(\text{PO}_4)_3$ and $\text{Na}_1\text{V}_2(\text{PO}_4)_3$ needs to be reinvestigated, in particular, providing structural information and the origin of the appearance of the intermediate $\text{Na}_2\text{V}_2(\text{PO}_4)_3$ phase.

Here, we elucidate the mechanisms of phase transition of the $\text{Na}_3\text{V}_2(\text{PO}_4)_3-\text{Na}_1\text{V}_2(\text{PO}_4)_3$ system including the intermediate $\text{Na}_2\text{V}_2(\text{PO}_4)_3$ phase, utilizing a $\text{V}^{4+/3+}$ redox couple. We also investigate the $\text{Na}_3\text{V}_2(\text{PO}_4)_3-\text{Na}_4\text{V}_2(\text{PO}_4)_3$ system involving the $\text{V}^{3+/2+}$ redox couple. The intermediate $\text{Na}_2\text{V}_2(\text{PO}_4)_3$ phase was detected by *operando* X-ray synchrotron diffraction and predicted by theoretical calculations. Here, we report for the first time on the crystal structure of the $\text{Na}_2\text{V}_2(\text{PO}_4)_3$ phase, compared in detail with those of $\text{Na}_x\text{V}_2(\text{PO}_4)_3$ ($x = 1, 3$, and 4). The intermediate $\text{Na}_2\text{V}_2(\text{PO}_4)_3$ phase appears as reducing the lattice mismatch between $\text{Na}_3\text{V}_2(\text{PO}_4)_3$ and $\text{Na}_1\text{V}_2(\text{PO}_4)_3$ phases and as the $\text{Na}(1)$ and $\text{Na}(2)$ sites split into several positions with different Na^+ distributions, including vacancies. This study is highly relevant to better understand the behavior of fast-rate electrode materials that display transient phases, such as the intermediate Li_xFePO_4 phases ($x = 0.6-0.75$) detected during non-equilibrium battery operations.²⁸⁻³⁶

■ EXPERIMENTAL SECTION

Synthesis. Carbon-coated $\text{Na}_3\text{V}_2(\text{PO}_4)_3$ was prepared by a sol-gel-assisted solid-state reaction. Na_2CO_3 (Sigma-Aldrich, 99.5%), $\text{C}_{10}\text{H}_{14}\text{O}_5\text{V}$ (Sigma-Aldrich, 97%), $\text{NH}_4\text{H}_2\text{PO}_4$ (Sigma-Aldrich, 98.5%), and citric acid (Alfa Aesar, 99%) in a molar ratio of 1.5:2:3:2 were dissolved in deionized water and ethanol (50/50 by volume). The solution was stirred overnight at 80 °C in an oil bath before being dried in an oven. The obtained powder was ground and preheated at 400 °C for 4 h in Ar. The resulting powder was then mixed in a mortar and annealed at 700 °C for 10 h under an Ar/H₂ (95/5) atmosphere.

Material Characterization. The chemical composition of the synthesized material was quantified using inductively coupled plasma optical emission spectroscopy (ICP-OES) with a Varian model 720-ES spectrometer. The standard solutions of Na (Agilent, 1001 ± 2 mg/L), V (SCP Science, 1004 ± 5 mg/L), and P (SCP Science, 1003 ± 5 mg/L) were used for calibrations. The amount of carbon coating on the synthesized material was measured by thermogravimetric analyses (TGAs) with a NETZSCH STA 449C. The morphology of the powder was examined by scanning electron microscopy (SEM) with a Hitachi Model S-4500 microscope.

Operando Synchrotron X-ray Diffraction. Operando synchrotron X-ray powder diffraction (SXRPD) measurements were performed on the MSPD beamline of the ALBA synchrotron in Spain³⁷ with Debye-Scherrer geometry ($\lambda = 0.8266 \text{ \AA}$) using an *in situ* coin cell with glass windows. Prior to the *operando* measurements, the SXRPD pattern of pristine $\text{Na}_3\text{V}_2(\text{PO}_4)_3$ was collected with a 0.3 mm diameter capillary. Two *in situ* cells containing $\text{Na}_3\text{V}_2(\text{PO}_4)_3$ electrodes were measured at the same time thanks to the eight-cell holder with an automatic positioning system available at the MSPD beamline.³⁸ Each SXRPD pattern was collected every 30 min with an acquisition time of ~3.5 min in the 2θ angular range of 2–40°, with a 2θ step size of 0.006° using a MYTHEN detector for rapid pattern collection. The working electrodes were composed of $\text{Na}_3\text{V}_2(\text{PO}_4)_3$ powder and carbon black (80/20 in wt %), and the Na metal was used as a counter/reference electrode. The mass loadings of the active material in the electrodes were 5.33 and 6.12 mg, respectively. One sheet of Whatman glass fiber (GF/D) was used as a separator and the electrolyte was composed of 1 M NaPF_6 in ethylene carbonate (EC)/dimethyl carbonate (DMC) (1:1, w/w) with 2 wt % of fluoroethylene carbonate (FEC). The first cell was measured for one cycle with a slow electrochemical reaction rate of 0.11 C (1 C = 58.2 mA/g or

about 9 h for the exchange of $1\text{Na}^+/1\text{e}^-$) with a voltage window of 1–3.75 V versus Na^+/Na . The second cell was measured for six cycles with higher C-rates (i.e., 0.37–0.77–0.77–0.77–0.37–0.77 C). A large overpotential was observed during the measurements of the second cell; hence, the voltage windows were adjusted with the respected C-rates (detailed cycling conditions can be found in Table S1 in the Supporting Information section).

Density Functional Theory Calculations. To assess the thermodynamic stability of $\text{Na}_x\text{V}_2(\text{PO}_4)_3$ with distinct Na-vacancy orderings at 0 K, we used spin-polarized density functional theory (DFT), as implemented in VASP.^{39,40} The exchange–correlation was approximated by the strongly constrained and appropriately normed (SCAN) metageneralized gradient approximation functional,⁴¹ with a U correction of 1.0 eV on all vanadium atoms to improve the localization of 3d electrons.⁴² The total energies were converged to within 10^{-5} eV/cell, atomic forces (stresses) within 10^{-2} eV/Å (0.29 GPa). The first Brillouin zone was integrated over a Γ -centered k -point grid of $3 \times 3 \times 3$ for all primitive structures containing two formula units (f.u.) with 42 atoms, a $1 \times 3 \times 3$ k -point mesh for all supercells with 4 f.u. (84 atoms), and a $1 \times 1 \times 3$ mesh for 8 f.u. (168 atoms). The valence electrons were treated in terms of plane waves up to an energy cutoff of 520 eV, while projector augmented wave potentials were used to describe the core electrons,⁴³ with Na 3s¹, V_pv 3p⁶3d⁴4s¹, P 2s²3p³, and O 2s²2p⁴.

The average intercalation voltage was derived using eq 1.

$$V = -\frac{\Delta G^0}{yF} \approx -\frac{E(\text{Na}_{x+y}\text{V}_2(\text{PO}_4)_3) - [E(\text{Na}_x\text{V}_2(\text{PO}_4)_3) + y\mu_{\text{Na}}]}{yF} \quad (1)$$

where ΔG^0 is the change in Gibbs free energy, as approximated from our DFT total energies, which ignore the zero-point energy correction, the pV term, and entropic effects. Thus, $E(\text{Na}_{x+y}\text{V}_2(\text{PO}_4)_3)$, $E(\text{Na}_x\text{V}_2(\text{PO}_4)_3)$, and μ_{Na} are the DFT total energies of stable Na-vacancy orderings at compositions $x+y$ and x and the chemical potential of the Na metal, respectively. F is the Faraday constant. Mixing enthalpies (H_{mixing}) at different Na compositions to construct the 0 K phase diagram were defined in eq 2.

$$H_{\text{mixing}}(x) \approx E[\text{Na}_x\text{V}_2(\text{PO}_4)_3] - \left(\frac{4-x}{3}\right)E[\text{Na}_1\text{V}_2(\text{PO}_4)_3] - \left(\frac{x-1}{3}\right)E[\text{Na}_4\text{V}_2(\text{PO}_4)_3] \quad (2)$$

■ RESULTS AND DISCUSSION

The composition of the as-synthesized $\text{Na}_3\text{V}_2(\text{PO}_4)_3$ powder was determined by elemental analysis using ICP-OES. The Na/V/P ratio was found to be 3.03(2):1.97(3):2.99(6), suggesting that the target composition $\text{Na}_3\text{V}_2(\text{PO}_4)_3$ was achieved through the sol-gel-assisted solid-state reaction. SEM images of the $\text{Na}_3\text{V}_2(\text{PO}_4)_3$ powder (Figure S1) show that the particles have no particular shapes as similar to other studies.^{11–13,17–22} However, relatively large agglomerates ranging from few microns to several tens of microns were found with the primary particles in the size of a few hundreds of nanometers. The powder is carbon-coated on the surface, ca. 9 wt % of carbon as determined by TGA measurements in air, as shown in Figure S2.

The SXRPD pattern of the as-synthesized $\text{Na}_3\text{V}_2(\text{PO}_4)_3$ powder is shown in Figure 1. No impurity phases were detected based on XRD analysis. As previously reported,⁴⁴ at room temperature, the crystal structure of $\text{Na}_3\text{V}_2(\text{PO}_4)_3$ cannot be indexed using a rhombohedral (*R*-3c) cell, but a monoclinic distortion must be considered. This is illustrated by

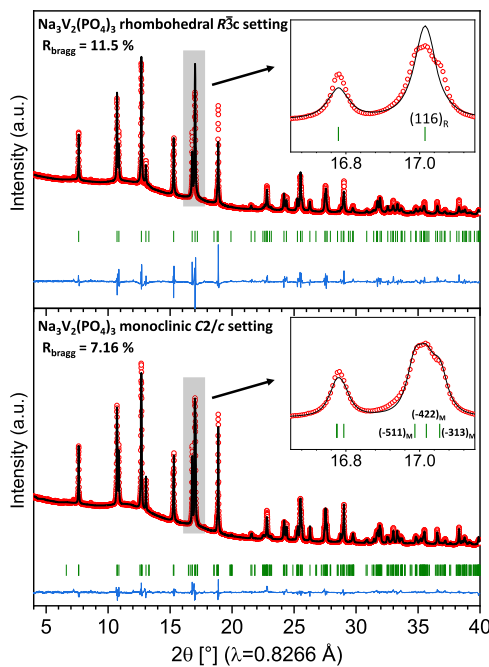


Figure 1. Rietveld refinement results of the as-synthesized $\text{Na}_3\text{V}_2(\text{PO}_4)_3$ powder with (top) the space group $R\bar{3}c$ and (bottom) the space group $C2/c$. The corresponding SXRPD pattern was collected at 298 K. It clearly shows that the structure of $\text{Na}_3\text{V}_2(\text{PO}_4)_3$ contains a monoclinic distortion as, for instance, $(116)_R$ reflection splits into $(-511)_M$, $(-422)_M$, and $(-313)_M$ (R and M here stand for rhombohedral and monoclinic, respectively).

the splitting of the $(116)_{\text{rhombohedral}}$ reflection at $d_{hkl} \sim 2.8 \text{ \AA}$ into $(-511)_{\text{monoclinic}}$, $(-422)_{\text{monoclinic}}$, and $(-313)_{\text{monoclinic}}$, which are signatures of the monoclinic distortion (inset images of Figure 1). Depending on the thermal history of the sample, $\text{Na}_3\text{V}_2(\text{PO}_4)_3$ can crystallize either in the monoclinic α or β form at room temperature (the reversible phase transition occurring very close to room temperature with about 10° of hysteresis).⁴⁴ In the present study, the crystal structure was refined with the monoclinic β phase since the (111) reflection at 6.74° ($\lambda = 0.8266 \text{ \AA}$) was not observed, while it is allowed in the α (i.e., Na^+ ordered) phase, as shown in Figure S3. The refined cell parameters using the Rietveld method are $a = 15.4104(4) \text{ \AA}$, $b = 8.7288(2) \text{ \AA}$, $c = 8.8257(2) \text{ \AA}$, $\beta = 126.1202(17)^\circ$, and $V/Z = 239.75(2) \text{ \AA}^3$ with the space group $C2/c$. The weak unindexed satellite reflections at low angles are attributed to an incommensurate modulated structure. These modulations originate both from the occupancies and the positions of Na^+ ions in $\text{Na}_3\text{V}_2(\text{PO}_4)_3$. No detailed structural study of the incommensurate β phase has been reported yet, and thus, the SXRPD pattern was refined without modulation vectors.

To study the (de-)intercalated phases and the Na^+ insertion/extraction mechanisms in $\text{Na}_3\text{V}_2(\text{PO}_4)_3$, *operando* SXRPD measurements were performed. Figure 2a displays a 2D view of SXRPD of a selected 2θ range during the first electrochemical charge–discharge cycle together with the corresponding galvanostatic data measured within a voltage window of 1.0–3.75 V (vs Na^+/Na) at a C-rate of $\sim 0.11 \text{ C}$ (for a wider 2θ range, see Figure S4). A total number of 89 scans were recorded during the first cycle. From scan number 1 to 30, $\text{Na}_3\text{V}_2(\text{PO}_4)_3$ is first oxidized up to 3.75 V versus Na^+/Na . During the charge process, two Na^+ cations are extracted

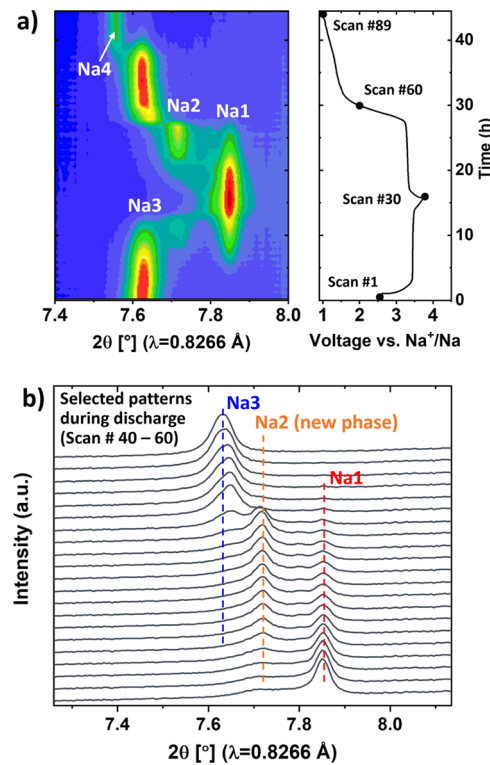


Figure 2. (a) *Operando* SXRPD patterns using $\text{Na}_3\text{V}_2(\text{PO}_4)_3$ as a positive electrode material in a half-cell versus Na metal upon charge and discharge, with a voltage window of 1.0–3.75 V versus Na^+/Na at a C-rate of 0.11 C ($\approx 1 \text{ Na}^+$ in 9 h). (b) Selected SXRPD patterns (from scan number 40–60 during discharge), where the intermediate $\text{Na}_2\text{V}_2(\text{PO}_4)_3$ phase appears more clearly. Na_x ($x = 1, 2$, and 3) refers to $\text{Na}_x\text{V}_2(\text{PO}_4)_3$.

leading to the composition $\text{Na}_1\text{V}_2(\text{PO}_4)_3$. Close to the mid-charge (i.e., after approximately 10 h of cycling), a weak reflection at $2\theta \approx 7.7^\circ$ starts to appear together with the presence of $\text{Na}_3\text{V}_2(\text{PO}_4)_3$ (corresponding reflection at $2\theta \approx 7.63^\circ$) and $\text{Na}_1\text{V}_2(\text{PO}_4)_3$ (corresponding reflection at $2\theta \approx 7.85^\circ$). $\text{Na}_1\text{V}_2(\text{PO}_4)_3$ is then reduced back to $\text{Na}_3\text{V}_2(\text{PO}_4)_3$ (scan number 60) and further to $\text{Na}_4\text{V}_2(\text{PO}_4)_3$ (scan number 89) at a potential of $\sim 1 \text{ V}$ versus Na^+/Na . During the discharge process, the very same peak at $2\theta \approx 7.7^\circ$ reappears with an increased intensity. This new reflection that is attributed to the new intermediate $\text{Na}_2\text{V}_2(\text{PO}_4)_3$ phase can be more clearly seen in the selected SXRPD patterns (scan number 40–60) of Figure 2b. As previously reported by Zakharkin et al.,²⁰ the appearance of the $\text{Na}_2\text{V}_2(\text{PO}_4)_3$ phase indicates that the electrochemical mechanisms of Na^+ insertion/extraction in $\text{Na}_3\text{V}_2(\text{PO}_4)_3$, involving the $\text{V}^{4+/3+}$ redox couple at $\sim 3.4 \text{ V}$ (vs Na^+/Na), are different from most of the existing reports.^{13,17–22}

The intermediate $\text{Na}_2\text{V}_2(\text{PO}_4)_3$ phase tended to coexist with the $\text{Na}_3\text{V}_2(\text{PO}_4)_3$ and $\text{Na}_1\text{V}_2(\text{PO}_4)_3$ phases at a low C-rate (0.11 C). However, when a higher current density was applied (i.e., toward a nonequilibrium state), the $\text{Na}_2\text{V}_2(\text{PO}_4)_3$ phase became more isolated. Similarly, in the operando study of LiFePO_4 , a higher C-rate (1 to 10 C) allowed a more intense appearance of the intermediate Li_xFePO_4 phase.³⁰ Even though the C-rates used in this study were relatively low, the battery cells already reached a nonequilibrium condition. This is probably because (i) the $\text{Na}_3\text{V}_2(\text{PO}_4)_3$ powder contains relatively large particles (see Figure S1) and (ii) the electrodes

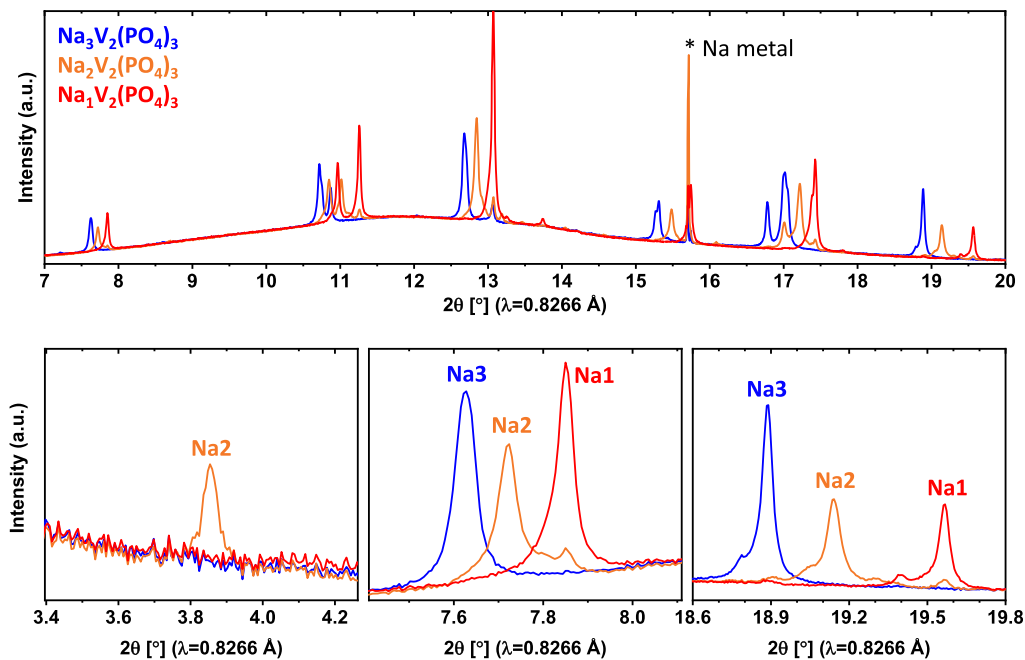


Figure 3. SXRPD patterns of $\text{Na}_3\text{V}_2(\text{PO}_4)_3$ (blue), $\text{Na}_2\text{V}_2(\text{PO}_4)_3$ (orange), and $\text{Na}_1\text{V}_2(\text{PO}_4)_3$ (red) with different angular domains. The Bragg peak at 3.85° is only observed for the new $\text{Na}_2\text{V}_2(\text{PO}_4)_3$ phase. The overall positions of the Bragg peaks manifest the appearance of the intermediate phase which can be differentiated from $\text{Na}_3\text{V}_2(\text{PO}_4)_3$ and $\text{Na}_1\text{V}_2(\text{PO}_4)_3$ phases.

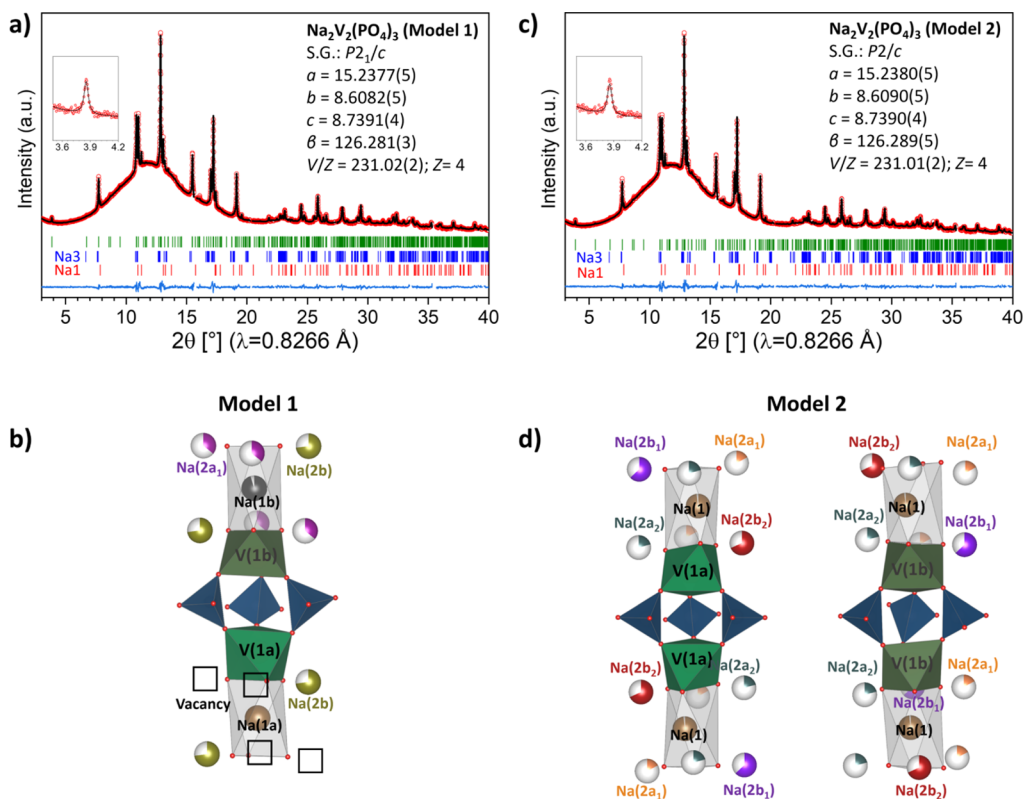


Figure 4. Rietveld refinement results of the intermediate phase $\text{Na}_2\text{V}_2(\text{PO}_4)_3$ using the (a) space group $P2_1/c$ (model 1) and (b) space group $P2/c$ (model 2). (c) Lantern unit with adjacent Na^+ ions in the crystal structure of $\text{Na}_2\text{V}_2(\text{PO}_4)_3$, refined with the space group $P2_1/c$. $\text{V}(1a)$ and $\text{V}(1b)$ atoms are involved in a single lantern unit. Vacant Na^+ positions are shown as empty squares. (d) Lantern units with adjacent Na^+ ions in the crystal structure of $\text{Na}_2\text{V}_2(\text{PO}_4)_3$, refined with the space group $P2/c$. Two different lantern units exist in the structure: each vanadium position forms a distinct lantern unit.

without a binder can induce a higher overpotential.⁴⁵ This is further confirmed by the observation of the large polarization of ~ 150 mV using the *in situ* cell compared to a low

polarization of 30 mV observed using a normal coin cell, cycled at the same C-rate of 0.11 C (Figure S5). Figure S6 shows *operando* SXRPD data collected during six cycles with the C-

Table 1. Refined Structural Parameters of the Intermediate Phase $\text{Na}_2\text{V}_2(\text{PO}_4)_3$ Using the Space Group $P2_1/c$ (Model 1)

atom	Wyckoff position	x/a	y/b	z/c	$U_{\text{iso}}, \text{\AA}^2$	Occ.
$\text{Na}_2\text{V}_2(\text{PO}_4)_3$						
	space group: $P2_1/c$ (#14); $Z = 4$					
	$a = 15.2377(5) \text{\AA}$; $b = 8.6082(5) \text{\AA}$; $c = 8.7391(4) \text{\AA}$; $\beta = 126.281(3)$;					
	$V = 924.069(8) \text{\AA}^3$; $V/Z = 231.02(2) \text{\AA}^3$					
	$R_{\text{wp}} = 13.3\%$; $R_p = 19.5\%$; $R_{\text{bragg}} = 6.21\%$					
V(1a)	4e	0.848(2)	0.492(5)	0.630(4)	0.026(3)	1
V(1b)	4e	0.640(2)	0.493(5)	0.834(4)	0.026(3)	1
P(1a)	4e	0.1047(10)	0.3521(17)	0.958(2)	0.033(4)	1
P(1b)	4e	0.3965(10)	0.3581(17)	0.564(2)	0.033(4)	1
P(2)	4e	0.2572(10)	0.7725(14)	0.262(2)	0.033(4)	1
O(1b)	4e	0.397(7)	0.372(10)	0.389(7)	0.012(3)	1
O(1d)	4e	0.094(7)	0.423(7)	0.107(10)	0.012(3)	1
O(1e)	4e	0.338(5)	0.700(10)	0.230(10)	0.012(3)	1
O(2b)	4e	0.208(6)	0.637(5)	0.303(10)	0.012(3)	1
O(2c)	4e	0.706(5)	0.916(10)	0.960(14)	0.012(3)	1
O(2f)	4e	0.805(5)	0.926(10)	0.547(14)	0.012(3)	1
O(1a)	4e	0.398(7)	0.319(2)	0.081(14)	0.012(3)	1
O(1c)	4e	0.104(7)	0.325(2)	0.478(10)	0.012(3)	1
O(1f)	4e	0.004(5)	0.085(10)	0.270(7)	0.012(3)	1
O(2a)	4e	0.506(5)	0.083(10)	0.240(7)	0.012(3)	1
O(2d)	4e	0.331(7)	0.614(10)	0.927(10)	0.012(3)	1
O(2e)	4e	0.167(6)	0.639(10)	0.582(7)	0.012(3)	1
Na(1a)	2a	0	0	0	0.090(13)	1 ^a
Na(1b)	2d	0.5	0	0.5	0.090(13)	0.98(8)
Na(2a ₁)	4e	0.557 ^a	0.168 ^a	0.908 ^a	0.090(13)	0.36(7)
Na(2a ₂)	4e	0.936	0.169	0.565	0.090(13)	0 ^a
Na(2b)	4e	0.232(7)	0.140(14)	0.243(14)	0.090(13)	0.73(10)

^aRevised and fixed at the last stages of refinement.

rates of 0.37–0.77–0.77–0.77–0.37–0.77 C (which are about three to seven times higher current densities than 0.11 C). To increase the chance of isolating a “pure” $\text{Na}_2\text{V}_2(\text{PO}_4)_3$ phase, multiple cycles were measured. The SXRPD pattern which appears mostly composed by the $\text{Na}_2\text{V}_2(\text{PO}_4)_3$ phase was obtained during the last cycle (see Figure S6 for more details).

Figure 3 shows a comparison of the SXRPD patterns among the $\text{Na}_x\text{V}_2(\text{PO}_4)_3$ ($x = 1, 2$, and 3) compositions. The strong background in the SXRPD patterns originates from the cell components, such as the electrolyte and the glass windows.⁴⁵ Importantly, a careful evaluation of the SXRPD pattern of $\text{Na}_2\text{V}_2(\text{PO}_4)_3$ reveals the appearance of a weak Bragg peak at a very low 2θ angle ($\sim 3.85^\circ$, $d_{hkl} = 12.29 \text{\AA}$). Through an *operando* technique, this weak Bragg peak at such a low angle (equivalent to $\sim 7.2^\circ$ in Cu $\text{K}\alpha$ radiation) may be missed with standard laboratory X-ray equipment, while we clearly observed it with a synchrotron X-ray source. This provides critical information to solve the crystal structure of $\text{Na}_2\text{V}_2(\text{PO}_4)_3$.

The powder pattern of $\text{Na}_2\text{V}_2(\text{PO}_4)_3$ presented in Figure 3 was then used to solve its crystal structure. The indexing of the powder pattern, the space group determination, and the cell transformation with group–subgroup relationships were carried out using Dicvol,⁴⁶ Chekcell,⁴⁷ and POWDERCELL⁴⁸ software, to fully resolve the crystal structure of $\text{Na}_2\text{V}_2(\text{PO}_4)_3$. During the steps of indexing and space group determination, it was found that the reflection at $2\theta = 3.85^\circ$ excludes the rhombohedral lattices (Figure S7) and C-centered monoclinic-type cells (Figure S8). Possible space groups are then primitive, and thus, several structure models with different space groups were examined to solve the structure. The initial

atomic positions of each model were deduced from the group–subgroup relationships starting from the $R-3c$ rhombohedral cell. The highest-to-lowest symmetries of the examined space groups are $P2_1/c$, $P2/c$, $P2_1/m$, and P/m (corresponding to 22, 23, 42, and 46 independent atoms per cell, respectively). We attempted unsuccessfully to solve the structure using the two space groups ($P2_1/m$ and P/m). The structure model, namely, “model 1”, using the $P2_1/c$ space group showed slightly better results than that using a $P2/c$ space group (i.e., model 2). The detailed comparisons between models 1 and 2 are discussed later in this paper.

For the structure of $\text{Na}_2\text{V}_2(\text{PO}_4)_3$ using the space group $P2_1/c$ (model 1), the refined cell parameters are $a = 15.2377(5) \text{\AA}$, $b = 8.6082(5) \text{\AA}$, $c = 8.7391(4) \text{\AA}$, $\beta = 126.281(3)$, and $V/Z = 231.02(2) \text{\AA}^3$. The results of Rietveld refinement are presented in Figure 4a, illustrating that the reflection at $2\theta = 3.85^\circ$ can be fully explained. The final refinement was performed using $\text{Na}_3\text{V}_2(\text{PO}_4)_3$ and $\text{Na}_1\text{V}_2(\text{PO}_4)_3$ as secondary phases with final weight fractions of 8.4(5) and 7.1(3)%, respectively. The global structural information, including atomic coordinates, atomic displacement parameters, and occupancy factors, is listed in Table 1. The crystal structure of $\text{Na}_2\text{V}_2(\text{PO}_4)_3$ contains two different vanadium Wyckoff positions, V(1a) and V(1b), involved in the same lantern unit, as illustrated in Figure 4b. From the examination of the V–O bond distances (Table S2), it appears that the environment of both V(1a) and V(1b) is similar with an average V–O bond distance of 1.99(9) \AA , which suggests that V^{3+} and V^{4+} are randomly distributed over the V(1a) and V(1b) positions. For the Na crystallographic sites, the Na(1) and Na(2) sites split into two Na(1) [labeled Na(1a) and

$\text{Na}(1\text{b})$] and three $\text{Na}(2)$ positions [labeled $\text{Na}(2\text{a}_1)$, $\text{Na}(2\text{a}_2)$, and $\text{Na}(2\text{b})$] in the space group $P2_1/c$. The refined occupancy factor for the $\text{Na}(2\text{a}_2)$ position was 0.08(7), which can be considered as fully empty. The refined occupancy factors for $\text{Na}(1\text{a})$, $\text{Na}(1\text{b})$, $\text{Na}(2\text{a}_1)$, and $\text{Na}(2\text{b})$ are 1, 0.98(8), 0.36(7), and 0.73(10), respectively, yielding a composition $\text{Na}_{2.1(3)}\text{V}_2(\text{PO}_4)_3$.

We tested another structural model for $\text{Na}_2\text{V}_2(\text{PO}_4)_3$ using the space group $P2/c$ (model 2), which showed similar agreement factors with the following cell parameters: $a = 15.2380(5) \text{ \AA}$; $b = 8.6090(5) \text{ \AA}$; $c = 8.7390(4)$; $\beta = 126.289(5)$, and $V/Z = 231.01(2) \text{ \AA}^3$ (Figure 4c). Model 2 also contains two vanadium positions, but it generates two distinct lantern units in the structure: one with two $\text{V}(1\text{a})$ atoms and the other one with two $\text{V}(1\text{b})$ atoms (Figure 4d). Furthermore, the average V–O distances in $\text{V}(1\text{a})\text{O}_6$ and $\text{V}(1\text{b})\text{O}_6$ octahedra are 1.92(8) and 2.04(8) \AA , respectively, suggesting a possible charge ordering of V^{4+} and V^{3+} in the crystal structure (see the details of V–O distances in Table S2). In terms of V charge ordering, model 2 compares well with the DFT data discussed below. Finally, the $\text{Na}(1)$ site is unique, while the $\text{Na}(2)$ site splits into four distinct Wyckoff positions, that is, $\text{Na}(2\text{a}_1)$, $\text{Na}(2\text{a}_2)$, $\text{Na}(2\text{b}_1)$, and $\text{Na}(2\text{b}_2)$. The refined occupancy factors for $\text{Na}(1)$, $\text{Na}(2\text{a}_1)$, $\text{Na}(2\text{a}_2)$, $\text{Na}(2\text{b}_1)$, and $\text{Na}(2\text{b}_2)$ are 0.98(3), 0.17(7), 0.21(7), 0.63(11), and 0.68(11), respectively, yielding a composition $\text{Na}_{2.0(3)}\text{V}_2(\text{PO}_4)_3$. Detailed structural information is listed in Table S3.

Note that both monoclinic structural models for $\text{Na}_2\text{V}_2(\text{PO}_4)_3$ ($P2/c$ and $P2_1/c$) have very similar cell parameters and can fully account for the existence of the (100) reflection at $2\theta = 3.85^\circ$. However, subtle differences to distinguish between the two space groups are convoluted in the possible existence of $[(0k0), k = 2n + 1]$ reflections for $P2/c$ while they are forbidden for $P2_1/c$. A very low-intensity peak at $\sim 5.5^\circ$ (of the SXRPD pattern) could be assigned to the (010) reflection in the space group $P2/c$, although the same was also observed in $\text{Na}_3\text{V}_2(\text{PO}_4)_3$ and $\text{Na}_1\text{V}_2(\text{PO}_4)_3$ phases with the same intensity. This evidence suggests that this peak may not originate from the phase reflection of $\text{Na}_x\text{V}_2(\text{PO}_4)_3$ but it is rather a noisy background (Figure S9). For this reason, we believe that the $P2_1/c$ model (model 1) is more suitable, although the $P2/c$ one (model 2) cannot be completely excluded.

To shed light on the thermodynamic stability of the intermediate $\text{Na}_2\text{V}_2(\text{PO}_4)_3$ phase, detected with our SXRPD diffraction, we performed dedicated DFT calculations. Figure 5 shows the thermodynamic properties of $\text{Na}_x\text{V}_2(\text{PO}_4)_3$ in the region of $x = 1–3$ at 0 K, as computed by DFT. Figure 5a shows the DFT mixing enthalpies (H_{mixing} in eq 2) for all Na/vacancy orderings of the $\text{Na}_x\text{V}_2(\text{PO}_4)_3$ compositions. Using a convex hull minimization algorithm, all the ground-state configurations were obtained. It can be concluded that besides the end members $\text{Na}_1\text{V}_2(\text{PO}_4)_3$ and $\text{Na}_3\text{V}_2(\text{PO}_4)_3$, which are assigned to rhombohedral and monoclinic symmetry, respectively, the new $\text{Na}_2\text{V}_2(\text{PO}_4)_3$ phase appears as a stable configuration. However, $\text{Na}_2\text{V}_2(\text{PO}_4)_3$ shows a relatively low mixing enthalpy (ca. -23 meV/f.u.) with respect to $\text{Na}_1\text{V}_2(\text{PO}_4)_3$ and $\text{Na}_3\text{V}_2(\text{PO}_4)_3$, and this suggests that the intermediate phase may be metastable at room temperature.

Table 2 presents unit cell parameters, sodium occupancy factors, and the average of V–O distances of the $\text{Na}_2\text{V}_2(\text{PO}_4)_3$ structure obtained by DFT calculations. The computed

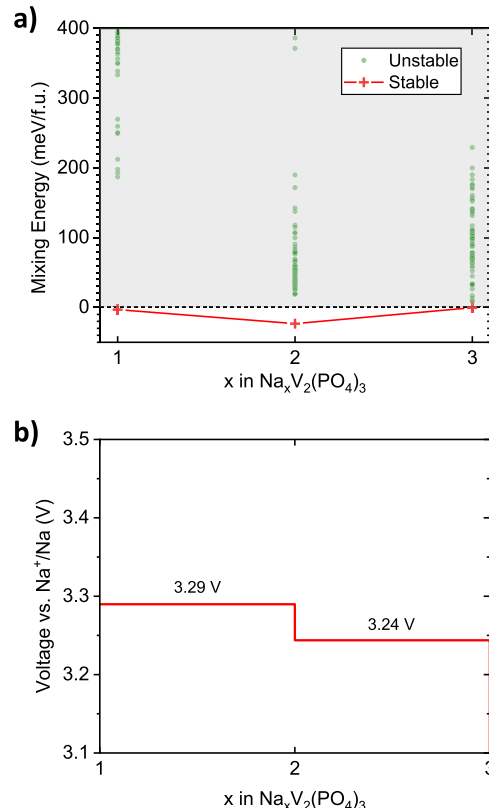


Figure 5. (a) DFT-derived phase diagram in the composition range ($1 \leq x \leq 3$) for $\text{Na}_x\text{V}_2(\text{PO}_4)_3$ at 0 K, in terms of Na mixing enthalpies. The stable ground-state configurations, namely, $\text{Na}_1\text{V}_2(\text{PO}_4)_3$, $\text{Na}_2\text{V}_2(\text{PO}_4)_3$, and $\text{Na}_3\text{V}_2(\text{PO}_4)_3$, and the unstable configurations are represented by red cross and green dots, respectively. (b) Computed voltage profile from $\text{Na}_1\text{V}_2(\text{PO}_4)_3$ to $\text{Na}_3\text{V}_2(\text{PO}_4)_3$.

structure of $\text{Na}_2\text{V}_2(\text{PO}_4)_3$ shows a similar cell volume with the experimentally observed one, and this calculated phase is assigned to a triclinic symmetry $P-1$ with distinguished V^{4+} and V^{3+} states and with fully ordered $\text{Na}(1)$ and $\text{Na}(2)$ sites. Higher temperatures will enable other Na-vacancy ordering to be stable, with intrinsic symmetries may be similar to what was found experimentally. Therefore, the structures extracted from the synchrotron measurements can be assumed with a superposition of several Na-vacancy orderings. A closer look to the local arrangement of Na ions in the DFT structure of $\text{Na}_2\text{V}_2(\text{PO}_4)_3$ shows that the fully occupied $\text{Na}(1)$ site is surrounded by two fully occupied $\text{Na}(2)$ sites and four vacancies.⁴⁹ Consequently, we could observe unique Na^+ sites of the $\text{Na}_2\text{V}_2(\text{PO}_4)_3$ ground state predicted by DFT split into a larger number of distinct Wyckoff positions compared to what was elaborated using our experimental model 1 and 2. However, our room-temperature synchrotron data of the intermediate $\text{Na}_2\text{V}_2(\text{PO}_4)_3$ structure detected under non-equilibrium conditions will likely incorporate several possible Na-vacancy configurations, averaging out the Na ions among the available $\text{Na}(1)$ and $\text{Na}(2)$ sites, which can be the origin of the observed fractional occupancies from SXRPD.^{44,50} Furthermore, our DFT calculations suggest a specific vanadium-charge orderings within the ground-state $\text{Na}_2\text{V}_2(\text{PO}_4)_3$, which may be disrupted by temperature effects. Ongoing synthesis efforts to obtain $\text{Na}_2\text{V}_2(\text{PO}_4)_3$ chemically as

Table 2. Unit Cell Parameters, Na Occupancy Factors, and Average of V–O Distances of $\text{Na}_2\text{V}_2(\text{PO}_4)_3$ Obtained by DFT Calculations

	S.G.	<i>a</i>	<i>b</i>	<i>c</i>	α	β	γ	V/Z	Na(1)/f.u.	Na(2)/f.u.	total Na/f.u.	avg. V–O (Å)
$\text{Na}_2\text{V}_2(\text{PO}_4)_3$	P-1	8.712	8.667	8.629	59.729	58.858	59.602	227.159	1	1	2	1.964

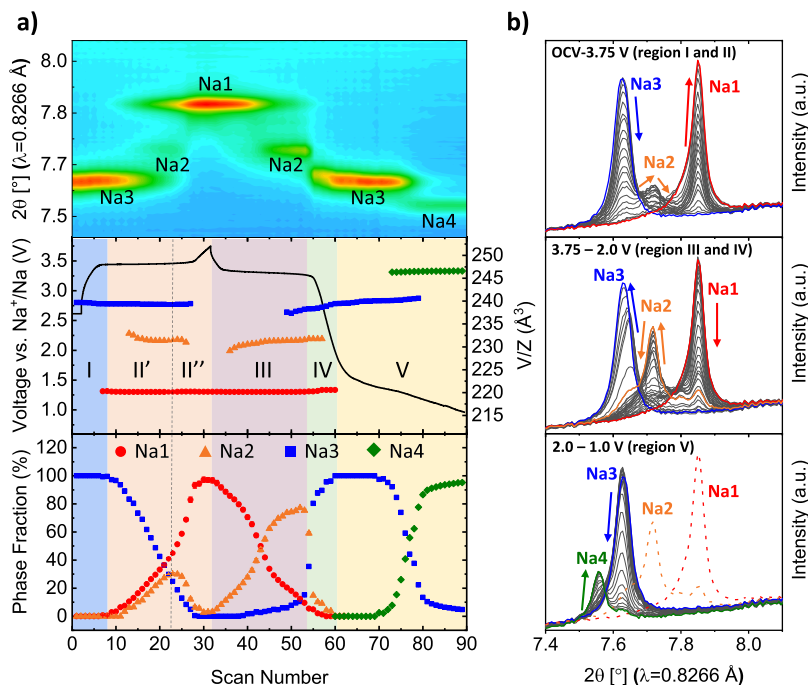


Figure 6. (a) Counter plot of *operando* SXRPD patterns in the 7.46–8.03° angular range (top). Voltage profile of $\text{Na}_3\text{V}_2(\text{PO}_4)_3$ during the first cycle, in a voltage window of 1.0–3.75 V vs Na^+/Na at a C-rate of 0.11 C and V/Z evolution of the $\text{Na}_x\text{V}_2(\text{PO}_4)_3$ ($x = 1, 2, 3$, and 4) phases (middle). The corresponding phase weights (bottom). (b) Details of the SXRPD patterns, upon Na^+ re-insertion from $\text{Na}_1\text{V}_2(\text{PO}_4)_3$ to $\text{Na}_3\text{V}_2(\text{PO}_4)_3$ (top), upon Na^+ extraction from $\text{Na}_3\text{V}_2(\text{PO}_4)_3$ to $\text{Na}_4\text{V}_2(\text{PO}_4)_3$ (bottom). Na_x ($x = 1, 2, 3$, and 4) refers to $\text{Na}_x\text{V}_2(\text{PO}_4)_3$.

a pure phase will further clarify the discrepancies between the DFT data and our experimental models.

Figure 5b depicts the DFT-derived voltage profile in the region of $\text{Na}_1\text{V}_2(\text{PO}_4)_3$ to $\text{Na}_3\text{V}_2(\text{PO}_4)_3$. By identifying the $\text{Na}_2\text{V}_2(\text{PO}_4)_3$ phase, we could realize two voltage plateaus while Na^+ intercalation via biphasic reaction mechanisms, namely, 3.29 V versus Na^+/Na between $\text{Na}_1\text{V}_2(\text{PO}_4)_3$ and $\text{Na}_2\text{V}_2(\text{PO}_4)_3$ and 3.24 V versus Na^+/Na between $\text{Na}_2\text{V}_2(\text{PO}_4)_3$ and $\text{Na}_3\text{V}_2(\text{PO}_4)_3$. Notably, the Na ordering of $\text{Na}_2\text{V}_2(\text{PO}_4)_3$ gives rise to a small voltage step (~50 mV).

Having the crystal structures of the new $\text{Na}_2\text{V}_2(\text{PO}_4)_3$ phase determined (with the space group $P2_1/c$), the *operando* SXRPD data collected upon cycling at a C-rate of 0.11 C (shown in Figure 2) were analyzed by Rietveld refinements including the evolutions of phase transitions, cell volumes, and phase weights, as shown in Figure 6. Five different regions can be distinguished during the charge and discharge processes (labeled from I to V) in Figure 6. In region I (solid solution part), only $\text{Na}_{3-\delta}\text{V}_2(\text{PO}_4)_3$ is present and its unit cell volume (V/Z) slightly decreases from 239.687(6) to 239.384(8) Å³, whereas the voltage increases from 2.61 to 3.44 V versus Na^+/Na . Region II (plateau at 3.4 V vs Na^+/Na) can be divided into two subregions (II' and II''). The Na^+ extraction mechanism occurs first through an out-of-equilibrium “three-phase” reaction, where the amount of the $\text{Na}_3\text{V}_2(\text{PO}_4)_3$ phase decreases while those of $\text{Na}_1\text{V}_2(\text{PO}_4)_3$ and $\text{Na}_2\text{V}_2(\text{PO}_4)_3$ phases increase concomitantly up to mid-charge (region II'). This can be rationalized as the overlap of two biphasic

reactions of $\text{Na}_3\text{V}_2(\text{PO}_4)_3$ – $\text{Na}_2\text{V}_2(\text{PO}_4)_3$ and $\text{Na}_2\text{V}_2(\text{PO}_4)_3$ – $\text{Na}_1\text{V}_2(\text{PO}_4)_3$. We note that the two reactions tend to separate more when higher current densities are furnished (Figure S6). After that (in region II''), the quantities of $\text{Na}_2\text{V}_2(\text{PO}_4)_3$ and $\text{Na}_3\text{V}_2(\text{PO}_4)_3$ phases diminish, while the $\text{Na}_1\text{V}_2(\text{PO}_4)_3$ content keeps increasing until the end of charge at ~3.75 V versus Na^+/Na . The discharge process down to ~2 V versus Na^+/Na appears rather different (region III). On the plateau, the main reaction seems to occur between $\text{Na}_1\text{V}_2(\text{PO}_4)_3$ and $\text{Na}_2\text{V}_2(\text{PO}_4)_3$ via a two-phase reaction. At this stage, the amount of $\text{Na}_3\text{V}_2(\text{PO}_4)_3$ remains low (<10 wt %). Afterward, in region IV, the phase transition from $\text{Na}_2\text{V}_2(\text{PO}_4)_3$ to $\text{Na}_3\text{V}_2(\text{PO}_4)_3$ occurred rapidly. Even though the voltage plateau at around 1.6 V versus Na^+/Na accompanies a slight sloping profile, in region V (reduction down to 1 V vs Na^+/Na), a biphasic reaction between $\text{Na}_3\text{V}_2(\text{PO}_4)_3$ and $\text{Na}_4\text{V}_2(\text{PO}_4)_3$ is observed. When the $\text{Na}_3\text{V}_2(\text{PO}_4)_3$ phase reappears during discharge, the reaction mainly occurs through a two-phase reaction mechanism. However, the slight peak shift to lower angles and the increase in V/Z observed in Figure 6b,a indicate that a partial solid solution mechanism is also involved. This behavior is typically observed not only in $\text{Na}_3\text{V}_2(\text{PO}_4)_3$ ^{17–22} but also in other electrode materials, such as $\text{Na}_3\text{Al}_{0.5}\text{V}_{1.5}(\text{PO}_4)_3$,⁵¹ $\text{Na}_4\text{MnCr}(\text{PO}_4)_3$,⁵² $\text{Na}_2\text{TiV}(\text{PO}_4)_3$,⁵³ and LiVOPO_4 ,⁵⁴ all including a two-phase reaction mechanism upon cycling. A major change in lattice parameters between the two end members of a two-phase reaction induces strains at the boundaries between these

Table 3. Unit Cell Parameters, Na Occupancy Factors, and Average V–O Distances for the Compositions $\text{Na}_x\text{V}_2(\text{PO}_4)_3$, ($x = 1, 2, 3$, and 4) Obtained by Rietveld Refinement^a

	S.G.	<i>A</i>	<i>B</i>	<i>c</i>	β	<i>V/Z</i>	Na(1)/f.u.	Na(2)/f.u.	Total Na/f.u.	Avg. V–O (Å)
$\text{Na}_4\text{V}_2(\text{PO}_4)_3$	<i>R</i> -3c	8.94302(10)	8.94302(10)	21.3609(4)	120	246.585(7)	0.97(4)	2.77(7)	3.74(11)	2.078(14)
$\text{Na}_3\text{V}_2(\text{PO}_4)_3$	<i>C</i> 2/ <i>c</i>	15.4065(3)	8.7288(2)	8.8243(2)	126.1091(16)	239.682(10)	0.679(14)	2.27(8)	2.9(1)	2.02(4)
$\text{Na}_2\text{V}_2(\text{PO}_4)_3$	<i>P</i> 2 ₁ / <i>c</i>	15.2377(5)	8.6082(5)	8.7391(4)	126.281(3)	231.02(2)	0.98(4)	1.2(3)	2.2(3)	1.99(9)
$\text{Na}_1\text{V}_2(\text{PO}_4)_3$	<i>R</i> -3c	8.42631(12)	8.42631(12)	21.4772(6)	120	220.105(8)	0.96(4)	0	0.96(4)	1.91(2)

^aSee the profiles of the Rietveld refinements for $\text{Na}_x\text{V}_2(\text{PO}_4)_3$ ($x = 1, 3$, and 4) in Figures S10–S12 and the details of their structural information in Tables S4–S6.

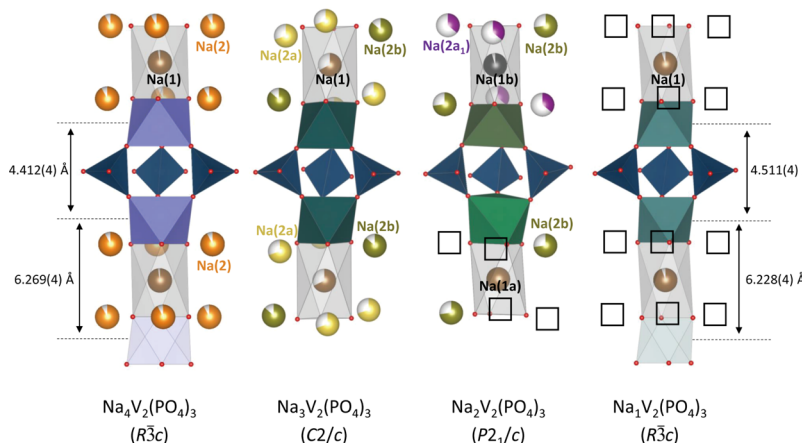


Figure 7. Illustration of the lantern units with adjacent Na ions of the compositions $\text{Na}_x\text{V}_2(\text{PO}_4)_3$ ($x = 1, 2, 3$, and 4). Black squares represent Na vacancies. The distances shown in $\text{Na}_4\text{V}_2(\text{PO}_4)_3$ and $\text{Na}_1\text{V}_2(\text{PO}_4)_3$ indicate V–V distances either through the Na(1) site or within the lantern unit.

two different domains and results in small changes in the cell parameters of the two end members as if a solid solution occurs.^{51,53,54} Nevertheless, the SXRPD pattern of $\text{Na}_3\text{V}_2(\text{PO}_4)_3$ is recovered after the re-sodiation, showing the high reversibility of the electrochemical reaction.

From the phase fraction analysis, it is clear that the $\text{Na}_2\text{V}_2(\text{PO}_4)_3$ phase could not be observed as completely isolated but rather coexisting together with the $\text{Na}_1\text{V}_2(\text{PO}_4)_3$ and $\text{Na}_3\text{V}_2(\text{PO}_4)_3$ ones. The maximum phase fraction of the $\text{Na}_2\text{V}_2(\text{PO}_4)_3$ phase observed during the charge was of 30.1(8) wt %, while it reached 77(1) wt % during discharge. The asymmetric behaviors in the appearance of the intermediate phase during charge and discharge were also observed in other studies of $\text{Na}_3\text{V}_2(\text{PO}_4)_3$ ^{18–20} and LiFePO_4 .^{30,32,35,36} The intermediate phases of $\text{Na}_x\text{V}_2(\text{PO}_4)_3$ and Li_xFePO_4 are more visible during charge in some cases^{18–20,30,36} and during discharge in other cases.^{20,32,35} Zakharkin et al. investigated three different synthesis routes for preparing $\text{Na}_3\text{V}_2(\text{PO}_4)_3$ with different precursors resulting in different intensities of the XRD reflections of the $\text{Na}_2\text{V}_2(\text{PO}_4)_3$ intermediate phase.²⁰ Depending on the synthesis procedures, the $\text{Na}_2\text{V}_2(\text{PO}_4)_3$ phase was either not observed, or observed only during charge, or observed during both charge and discharge.²⁰ These observations may suggest that the intermediate phase could be metastable/transient. Further investigations are required to understand the origin of the asymmetric behavior of the $\text{Na}_2\text{V}_2(\text{PO}_4)_3$ intermediate phase in the $\text{Na}_3\text{V}_2(\text{PO}_4)_3$ – $\text{Na}_1\text{V}_2(\text{PO}_4)_3$ system.

A global overview of cell parameters, Na site occupancies, and average of V–O bond lengths of $\text{Na}_x\text{V}_2(\text{PO}_4)_3$ ($x = 1, 2, 3$, and 4) is summarized in Table 3. For the monoclinic phases, $\text{Na}_3\text{V}_2(\text{PO}_4)_3$ and $\text{Na}_2\text{V}_2(\text{PO}_4)_3$, the *a*, *b*, and *c* parameters decrease by ~1.1, 1.38, and 0.97%, respectively, and a slight

increase in the β angle (0.14%) is noticed from $x = 3$ to 2 in $\text{Na}_x\text{V}_2(\text{PO}_4)_3$. The two end members ($\text{Na}_4\text{V}_2(\text{PO}_4)_3$ and $\text{Na}_1\text{V}_2(\text{PO}_4)_3$) crystallize in the same space group *R*-3c. From the Na-rich phase, $\text{Na}_4\text{V}_2(\text{PO}_4)_3$, to the Na-poor one, $\text{Na}_1\text{V}_2(\text{PO}_4)_3$, the *a* parameter dramatically decreases from 8.94302(10) to 8.42631(12) Å ($\Delta a/a = -5.81\%$), while the *c* parameter slightly increases from 21.3609(4) to 21.4772(6) Å ($\Delta c/c = 0.54\%$). This noticeable anisotropy in the change in cell parameters is closely linked to the occupancies of the Na(1) and Na(2) sites.

Generally, Na^+ insertion in the NASICON structure increases the *a* parameter and decreases the *c* parameter (in hexagonal axes). When the Na(1) site is depopulated, the *c* parameter increases mainly due to an increasing repulsion between parallel O_3 triangular faces of the MO_6 octahedra through the Na(1) site, as less screened by the Na^+ ions.^{15,52,55–57}

In the case of $\text{Na}_x\text{V}_2(\text{PO}_4)_3$, the distances between adjacent VO_6 octahedra through the Na(1) site along [001]hexagonal remain nearly constant, 6.269(4) Å in $\text{Na}_4\text{V}_2(\text{PO}_4)_3$ and 6.228(4) Å in $\text{Na}_1\text{V}_2(\text{PO}_4)_3$ (Figure 7), as the Na(1) site stays fully occupied [$0.96(4) \rightarrow 0.97(4)$ when x varies from 4 to 1 in $\text{Na}_x\text{V}_2(\text{PO}_4)_3$]. As a consequence, the *c* parameter undergoes no significant variation. The main reason for the slight increase in the *c* parameter may be the stronger repulsion of neighbors between VO_6 octahedra within the lantern unit when vanadium is oxidized from $\text{V}^{2.5+}$ to V^{4+} . Therefore, the V–V distances within the lantern unit themselves increase from 4.412(4) to 4.511(4) Å (Figure 7). Similar evolutions of the *a* and *c* cell parameters were found in other NASICON positive electrode materials but with a more pronounced increase in the *c* parameter: $\Delta a/a = -6.1\%$ and $\Delta c/c = 2.4\%$ in $\text{Na}_x\text{MnV}(\text{PO}_4)_3$ ¹⁵ and $\Delta a/a = -4.9\%$ and $\Delta c/c = 2.2\%$ in Na_xMnCr

$(\text{PO}_4)_3$ ⁵² when x varies from 4 to 1. Unlike the case of $\text{Na}_x\text{V}_2(\text{PO}_4)_3$, a much depopulated Na(1) site is observed in $\text{Na}_x\text{MnV}(\text{PO}_4)_3$ [from 1 to 0.49(1) when x varies from 4 to 1], inducing stronger repulsions between the $(\text{Mn}, \text{V})_6$ octahedra through the Na(1) site and thus a remarkable increase in the c parameter.^{15,55}

Overall, the value of V/Z gradually decreases with a decreasing number of Na^+ ions in the structure (driving a progressive oxidation of vanadium), from 246.585(7), to 239.682(10), to 231.02(2), and to 220.105(8) Å³ when x varies from 4 to 1 in $\text{Na}_x\text{V}_2(\text{PO}_4)_3$. The lattice mismatch in the phase transition between $\text{Na}_3\text{V}_2(\text{PO}_4)_3$ and $\text{Na}_1\text{V}_2(\text{PO}_4)_3$ ($\Delta V/V = 8.2\%$) is noticeably reduced when $\text{Na}_2\text{V}_2(\text{PO}_4)_3$ is invoked ($\Delta V/V = 3.6$ and 4.7%, for $\text{Na}_3\text{V}_2(\text{PO}_4)_3 \rightarrow \text{Na}_2\text{V}_2(\text{PO}_4)_3$ and $\text{Na}_2\text{V}_2(\text{PO}_4)_3 \rightarrow \text{Na}_1\text{V}_2(\text{PO}_4)_3$, respectively). The reduced lattice mismatch enables a rapid phase transition between $\text{Na}_3\text{V}_2(\text{PO}_4)_3$ and $\text{Na}_1\text{V}_2(\text{PO}_4)_3$ via $\text{Na}_2\text{V}_2(\text{PO}_4)_3$ by lowering their nucleation energies.³⁰

The average V–O bond distances consequently show a gradual decrease from 2.076(14), to 2.02(4), to 1.99(9), and to 1.91(2) Å when x in $\text{Na}_x\text{V}_2(\text{PO}_4)_3$ changes from 4 to 1. The details of (not average but individual) V–O bond distances in $\text{Na}_x\text{V}_2(\text{PO}_4)_3$ are shown in Table S2. Also, the volumes of the VO_6 octahedra decrease in parallel from 11.69, to 10.73, to 10.16, and to 9.15 Å³, respectively ($\Delta V_{\text{oct}}/V_{\text{oct}} = 21.7\%$). As a comparison, the volume of the $(\text{Mn}, \text{V})_6$ octahedra decreases about 23.8% when x varies from 4 to 1 in $\text{Na}_x\text{MnV}(\text{PO}_4)_3$.¹⁵ Furthermore, as x in $\text{Na}_x\text{V}_2(\text{PO}_4)_3$ decreases from 4 to 1, the average oxidation states of vanadium obtained by BVS calculation are 2.44(4), 2.92(11), 3.3(3), and 3.87(8), respectively, showing good agreement with the average vanadium oxidation states expected for each composition (i.e., 2.5, 3, 3.5, and 4, respectively).

When it comes to the number of Na^+ in the Na(1) and Na(2) sites per formula unit (Table 3), our findings establish that the Na(1) site is almost fully occupied in all compositions except for $\text{Na}_3\text{V}_2(\text{PO}_4)_3$ as the occupancy factor of the Na(1) site is 0.679(14). For the Na(2) site, when the Na^+ content changes from $x = 4$ to 1 in $\text{Na}_x\text{V}_2(\text{PO}_4)_3$, the occupancy factor gradually decreases from almost 100% down to ~0%. This evidence appears in good agreement with the computational analysis on Na(1) and Na(2) sites at room temperature.⁴⁹ Other NASICON-type materials also show similar trends, that is, the Na(1) site tends to keep its high occupancies, while the Na(2) site is populated or depopulated depending on the compositions.^{8,9,14–16} Overall, the refined total number of Na^+ per formula unit shows very good agreement with the expected compositions.

The detailed evolution on the Na^+ distributions around the lantern units of the four compositions [$\text{Na}_x\text{V}_2(\text{PO}_4)_3$, with $x = 1, 2, 3$, and 4] is illustrated in Figure 7. The Na(2) site in $\text{Na}_4\text{V}_2(\text{PO}_4)_3$ ($R-3c$) splits into the two Na(2) positions, Na(2a) and Na(2b), in $\text{Na}_3\text{V}_2(\text{PO}_4)_3$ ($C2/c$). Then, from $\text{Na}_3\text{V}_2(\text{PO}_4)_3$ to $\text{Na}_2\text{V}_2(\text{PO}_4)_3$ ($P2_1/c$), the Na(1) site splits into the Na(1a) and Na(1b) positions that are almost fully occupied in $\text{Na}_2\text{V}_2(\text{PO}_4)_3$. The Na(2a) position also further splits into Na(2a₁) and Na(2a₂) in $\text{Na}_2\text{V}_2(\text{PO}_4)_3$, but the Na(2a₂) is found to be empty. Finally, from $\text{Na}_2\text{V}_2(\text{PO}_4)_3$ to $\text{Na}_1\text{V}_2(\text{PO}_4)_3$, the structure is back to the rhombohedral unit cell ($R-3c$), having the Na(2) site fully emptied. It is interesting that from $\text{Na}_4\text{V}_2(\text{PO}_4)_3$ to $\text{Na}_2\text{V}_2(\text{PO}_4)_3$, the Na(2b) position tends to be more occupied than the Na(2a) positions. This may be related to different connectivities of Na(2a) and

Na(2b) with the Na(1) site. Figure 8 shows the polyhedra constructed from Na and O atoms in $\text{Na}_3\text{V}_2(\text{PO}_4)_3$ or

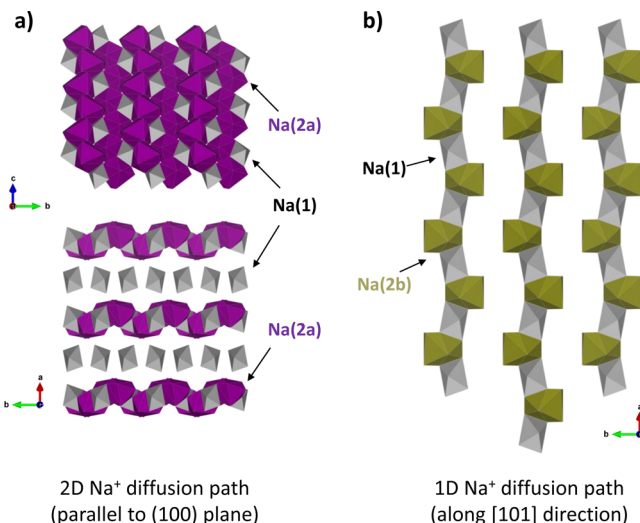


Figure 8. Different connectivities of (a) Na(2a) with Na(1) and (b) Na(2b) with Na(1) in $\text{Na}_3\text{V}_2(\text{PO}_4)_3$ or $\text{Na}_2\text{V}_2(\text{PO}_4)_3$. The polyhedra are constructed from Na and O atoms.

$\text{Na}_2\text{V}_2(\text{PO}_4)_3$. The connectivity between Na(2a) and Na(1) forms distinct 2D Na^+ diffusion paths parallel to the (100) plane, while the connectivity between Na(2b) and Na(1) results in 1D Na^+ diffusion chains along the [101] direction. Although a computational assessment of the migration barriers of Na ions in the $\text{Na}_3\text{V}_2(\text{PO}_4)_3$ or $\text{Na}_2\text{V}_2(\text{PO}_4)_3$ phases can support our structural analysis, we hypothesize that Na^+ ions in the Na(2a) position may show easier migration than those in the Na(2b) position, therefore explaining the lower occupancy factor observed for Na(2a) than Na(2b).

CONCLUSIONS

In this study, we report for the first time the crystal chemistry of the new intermediate $\text{Na}_2\text{V}_2(\text{PO}_4)_3$ composition and the electrochemical reaction mechanisms of $\text{Na}_x\text{V}_2(\text{PO}_4)_3$ ($1 \leq x \leq 4$) including the intermediate phase. The appearance of the $\text{Na}_2\text{V}_2(\text{PO}_4)_3$ phase occurs in a nonequilibrium battery operation and it is better observed with a higher current density (i.e., nonequilibrium state). The results of Rietveld refinement suggest that the crystal structure of $\text{Na}_2\text{V}_2(\text{PO}_4)_3$ crystallizes in a primitive (monoclinic) cell with the possible space groups of $P2_1/c$ (model 1) or $P2/c$ (model 2) rather than rhombohedral ($R-3c$) or monoclinic ($C2/c$) cells of other $\text{Na}_x\text{V}_2(\text{PO}_4)_3$ ($x = 1, 3$, and 4) compositions. The main difference between the two structure models proposed for $\text{Na}_2\text{V}_2(\text{PO}_4)_3$ is ascribed to different vanadium environments. As the symmetry is reduced in $\text{Na}_2\text{V}_2(\text{PO}_4)_3$, the vanadium site splits into two Wyckoff positions. The structure with the space group $P2_1/c$ (model 1) contains a single lantern unit with a random distribution of V^{3+} and V^{4+} types over two vanadium positions. The structure with the space group $P2/c$ (model 2) contains two different lantern units, each vanadium position forming its own lantern unit, with a possible charge ordering between V^{3+} and V^{4+} . For the sodium sites, the Na(1) site is almost fully occupied for both structure models. The Na(2) site splits into several positions, in which one of the splitting Na(2) position [Na(2a₂)] is found to be a vacancy in the

structure model 1, whereas the four splitting Na(2) positions are all partially filled in the structure model 2. The structure independently predicted by our DFT simulations at 0 K also shows a vanadium-charge ordering and a full Na⁺/vacancy ordering. A fully ordered Na⁺ at 0 K becomes partially ordered at room temperature. These different Na⁺ distributions suggest that the Na₂V₂(PO₄)₃ phase can have possible phase transitions versus temperature due to Na⁺ order/disorder phenomena. Furthermore, Na⁺ ions in the Na(2a) position may diffuse more easily than those in the Na(2b) position due to different connectivities with the Na(1) site. The intermediate Na₂V₂(PO₄)₃ phase appears by reducing the lattice mismatch between Na₃V₂(PO₄)₃ and Na₁V₂(PO₄)₃ phases lowering their nucleation energy thus beneficial for a high-rate performance. This study opens the door to a better understanding of the behavior of the Na₃V₂(PO₄)₃ electrode upon cycling when the intermediate phase is involved. We believe that our findings in this work will encourage researchers to further investigate the nature of the new Na₂V₂(PO₄)₃ phase.

■ ASSOCIATED CONTENT

§ Supporting Information

The Supporting Information is available free of charge at <https://pubs.acs.org/doi/10.1021/acs.chemmater.1c04033>.

SEM images, TGA, synchrotron powder XRD patterns, *operando* XRD data, and detailed crystallographic information ([PDF](#))

■ AUTHOR INFORMATION

Corresponding Authors

Pieremanuele Canepa — Department of Materials Science and Engineering, National University of Singapore, Singapore 117575, Singapore; Chemical and Biomolecular Engineering, National University of Singapore, 117585, Singapore; [orcid.org/0000-0002-5168-9253](#); Email: pcanepa@nus.edu.sg

Jean-Noël Chotard — Laboratoire de Réactivité et de Chimie des Solides, Université de Picardie Jules Verne, CNRS-UMR 7314, F-80039 Amiens Cedex 1, France; RS2E, Réseau Français sur le Stockage Electrochimique de l'Energie, FR CNRS 3459, F-80039 Amiens Cedex 1, France; [orcid.org/0000-0002-9867-7954](#); Email: jean-noel.chotard@u-picardie.fr

Authors

Sunkyu Park — Laboratoire de Réactivité et de Chimie des Solides, Université de Picardie Jules Verne, CNRS-UMR 7314, F-80039 Amiens Cedex 1, France; CNRS, University of Bordeaux, Bordeaux INP, ICMCB UMR 5026, F-33600 Pessac, France; TIAMAT, 80000 Amiens, France; [orcid.org/0000-0001-6706-7654](#)

Ziliang Wang — Department of Materials Science and Engineering, National University of Singapore, Singapore 117575, Singapore

Zeyu Deng — Department of Materials Science and Engineering, National University of Singapore, Singapore 117575, Singapore; [orcid.org/0000-0003-0109-9367](#)

Iona Moog — TIAMAT, 80000 Amiens, France
François Fauth — CELLS-ALBA Synchrotron, E-08290 Barcelona, Spain; [orcid.org/0000-0001-9465-3106](#)

Dany Carlier — CNRS, University of Bordeaux, Bordeaux INP, ICMCB UMR 5026, F-33600 Pessac, France; RS2E, Réseau Français sur le Stockage Electrochimique de l'Energie, FR CNRS 3459, F-80039 Amiens Cedex 1, France; [orcid.org/0000-0002-5086-4363](#)

Laurence Croguennec — CNRS, University of Bordeaux, Bordeaux INP, ICMCB UMR 5026, F-33600 Pessac, France; RS2E, Réseau Français sur le Stockage Electrochimique de l'Energie, FR CNRS 3459, F-80039 Amiens Cedex 1, France; [orcid.org/0000-0002-3018-0992](#)

Christian Masquelier — Laboratoire de Réactivité et de Chimie des Solides, Université de Picardie Jules Verne, CNRS-UMR 7314, F-80039 Amiens Cedex 1, France; RS2E, Réseau Français sur le Stockage Electrochimique de l'Energie, FR CNRS 3459, F-80039 Amiens Cedex 1, France; [orcid.org/0000-0001-7289-1015](#)

Complete contact information is available at:
<https://pubs.acs.org/10.1021/acs.chemmater.1c04033>

Notes

The authors declare no competing financial interest.

■ ACKNOWLEDGMENTS

The authors thank Emmanuel Petit (ICMCB) for SEM measurements and Matthieu Courty (LRCS) for TGA analysis. The authors also acknowledge ALBA (Barcelona, Spain) for synchrotron X-ray diffraction experiments on the MSPD beamline (proposal number 20200024218). S.P. acknowledges Jon Serrano for a fruitful discussion on Rietveld refinements. The authors are grateful to the ANRT and TIAMAT for the funding (CIFRE grant) of S.P.'s Ph.D. thesis. We acknowledge the financial support of Région Nouvelle Aquitaine and the French National Research Agency (STORE-EX Labex Project ANR-10-LABX-76-01). P.C., C.M., J.-N. C., and Z.D. are grateful to the ANR-NRF NRF2019-NRF-ANR073 NaMASTER. P.C. and Z.D. acknowledge funding from the National Research Foundation under the NRF Fellowship NRFF12-2020-0012. Part of the computational work was performed using resources of the National Supercomputing Centre, Singapore (<https://www.nscc.sg>).

■ REFERENCES

- (1) Masquelier, C.; Croguennec, L. Polyanionic (Phosphates, Silicates, Sulfates) Frameworks as Electrode Materials for Rechargeable Li (or Na) Batteries. *Chem. Rev.* **2013**, *113*, 6552–6591.
- (2) Hasa, I.; Mariyappan, S.; Saurel, D.; Adelhelm, P.; Koposov, A. Y.; Masquelier, C.; Croguennec, L.; Casas-Cabanas, M. Challenges of Today for Na-Based Batteries of the Future: From Materials to Cell Metrics. *J. Power Sources* **2021**, *482*, 228872.
- (3) Jian, Z.; Hu, Y. S.; Ji, X.; Chen, W. NASICON-Structured Materials for Energy Storage. *Adv. Mater.* **2017**, *29*, 1601925.
- (4) Chen, S.; Wu, C.; Shen, L.; Zhu, C.; Huang, Y.; Xi, K.; Maier, J.; Yu, Y. Challenges and Perspectives for NASICON-Type Electrode Materials for Advanced Sodium-Ion Batteries. *Adv. Mater.* **2017**, *29*, 1700431.
- (5) Rajagopalan, R.; Zhang, Z.; Tang, Y.; Jia, C.; Ji, X.; Wang, H. Understanding Crystal Structures, Ion Diffusion Mechanisms and Sodium Storage Behaviors of NASICON Materials. *Energy Storage Mater.* **2021**, *34*, 171–193.
- (6) Singh, B.; Wang, Z.; Park, S.; Gautam, G. S.; Chotard, J.-N.; Croguennec, L.; Carlier, D.; Cheetham, A. K.; Masquelier, C.; Canepa, P. A Chemical Map of NaSICON Electrode Materials for Sodium-Ion Batteries. *J. Mater. Chem. A* **2021**, *9*, 281–292.

- (7) Zhang, B.; Ma, K.; Lv, X.; Shi, K.; Wang, Y.; Nian, Z.; Li, Y.; Wang, L.; Dai, L.; He, Z. Recent Advances of NASICON-Na₃V₂(PO₄)₃ as Cathode for Sodium-Ion Batteries: Synthesis, Modifications, and Perspectives. *J. Alloys Compd.* **2021**, *867*, 159060.
- (8) Bui, K. M.; Dinh, V. A.; Okada, S.; Ohno, T. Hybrid Functional Study of the NASICON-Type Na₃V₂(PO₄)₃: Crystal and Electronic Structures, and Polaron-Na Vacancy Complex Diffusion. *Phys. Chem. Chem. Phys.* **2015**, *17*, 30433–30439.
- (9) Song, W.; Cao, X.; Wu, Z.; Chen, J.; Huangfu, K.; Wang, X.; Huang, Y.; Ji, X. A Study into the Extracted Ion Number for NASICON Structured Na₃V₂(PO₄)₃ in Sodium-Ion Batteries. *Phys. Chem. Chem. Phys.* **2014**, *16*, 17681–17687.
- (10) Saravanan, K.; Mason, C. W.; Rudola, A.; Wong, K. H.; Balaya, P. The First Report on Excellent Cycling Stability and Superior Rate Capability of Na₃V₂(PO₄)₃ for Sodium Ion Batteries. *Adv. Energy Mater.* **2013**, *3*, 444–450.
- (11) Zheng, Q.; Yi, H.; Li, X.; Zhang, H. Progress and Prospect for NASICON-Type Na₃V₂(PO₄)₃ for Electrochemical Energy Storage. *J. Energy Chem.* **2018**, *27*, 1597–1617.
- (12) Zhang, X.; Rui, X.; Chen, D.; Tan, H.; Yang, D.; Huang, S.; Yu, Y. Na₃V₂(PO₄)₃: An Advanced Cathode for Sodium-Ion Batteries. *Nanoscale* **2019**, *11*, 2556–2576.
- (13) Lim, S. Y.; Kim, H.; Shakoor, R. A.; Jung, Y.; Choi, J. W. Electrochemical and Thermal Properties of NASICON Structured Na₃V₂(PO₄)₃ as a Sodium Rechargeable Battery Cathode: A Combined Experimental and Theoretical Study. *J. Electrochem. Soc.* **2012**, *159*, A1393–A1397.
- (14) Kabbour, H.; Coillot, D.; Colmont, M.; Masquelier, C.; Mentré, O. α-Na₃M₂(PO₄)₃ (M = Ti, Fe): Absolute Cationic Ordering in NASICON-Type Phases. *J. Am. Chem. Soc.* **2011**, *133*, 11900–11903.
- (15) Chen, F.; Kovrugin, V. M.; David, R.; Mentré, O.; Fauth, F.; Chotard, J. N.; Masquelier, C. A NASICON-Type Positive Electrode for Na Batteries with High Energy Density: Na₄MnV(PO₄)₃. *Small Methods* **2018**, *3*, 1800218.
- (16) Wang, Q.; Zhang, M.; Zhou, C.; Chen, Y. Concerted Ion-Exchange Mechanism for Sodium Diffusion and Its Promotion in Na₃V₂(PO₄)₃ Framework. *J. Phys. Chem. C* **2018**, *122*, 16649–16654.
- (17) Zhang, G.; Xiong, T.; Yan, M.; Xu, Y.; Ren, W.; Xu, X.; Wei, Q.; Mai, L. In Operando Probing of Sodium-Incorporation in NASICON Nanomaterial: Asymmetric Reaction and Electrochemical Phase Diagram. *Chem. Mater.* **2017**, *29*, 8057–8064.
- (18) Yao, X.; Zhu, Z.; Li, Q.; Wang, X.; Xu, X.; Meng, J.; Ren, W.; Zhang, X.; Huang, Y.; Mai, L. 3.0 v High Energy Density Symmetric Sodium-Ion Battery: Na₄V₂(PO₄)₃||Na₃V₂(PO₄)₃. *ACS Appl. Mater. Interfaces* **2018**, *10*, 10022–10028.
- (19) Wei, C.; Luo, F.; Zhang, C.; Gao, H.; Niu, J.; Ma, W.; Bai, Y.; Zhang, Z. Voltage Window-Dependent Electrochemical Performance and Reaction Mechanisms of Na₃V₂(PO₄)₃ Cathode for High-Capacity Sodium Ion Batteries. *Ionics* **2020**, *26*, 2343–2351.
- (20) Zakharkin, M. V.; Drozhzhin, O. A.; Ryazantsev, S. V.; Chernyshov, D.; Kirsanova, M. A.; Mikheev, I. V.; Pazhetnov, E. M.; Antipov, E. V.; Stevenson, K. J. Electrochemical Properties and Evolution of the Phase Transformation Behavior in the NASICON-type Na_{3+x}Mn_xV_{2-x}(PO₄)₃ (0≤x≤1) Cathodes for Na-Ion Batteries. *J. Power Sources* **2020**, *470*, 228231.
- (21) Jian, Z.; Han, W.; Lu, X.; Yang, H.; Hu, Y.-S.; Zhou, J.; Zhou, Z.; Li, J.; Chen, W.; Chen, D.; et al. Superior Electrochemical Performance and Storage Mechanism of Na₃V₂(PO₄)₃ Cathode for Room-Temperature Sodium-Ion Batteries. *Adv. Energy Mater.* **2013**, *3*, 156–160.
- (22) Mirza, S.; Song, Z.; Zhang, H.; Hussain, A.; Zhang, H.; Li, X. A Simple Pre-Sodiation Strategy to Improve the Performance and Energy Density of Sodium Ion Batteries with Na₃V₂(PO₄)₃ as the Cathode Material. *J. Mater. Chem. A* **2020**, *8*, 23368–23375.
- (23) Uebo, Y.; Kiyabu, T.; Okada, S.; Yamaki, J. Electrochemical Sodium Insertion into the 3D-Framework of Na₃M₂(PO₄)₃ (M=Fe, V). *Rep. Inst. Adv. Mater. Study, Kyushu Univ.* **2002**, *16*, 1–5.
- (24) Li, G.; Jiang, D.; Wang, H.; Lan, X.; Zhong, H.; Jiang, Y. Glucose-Assisted Synthesis of Na₃V₂(PO₄)₃/C Composite as an Electrode Material for High-Performance Sodium-Ion Batteries. *J. Power Sources* **2014**, *265*, 325–334.
- (25) Lim, S.-J.; Han, D.-W.; Nam, D.-H.; Hong, K.-S.; Eom, J.-Y.; Ryu, W.-H.; Kwon, H.-S. Structural Enhancement of Na₃V₂(PO₄)₃/C Composite Cathode Materials by Pillar Ion Doping for High Power and Long Cycle Life Sodium-Ion Batteries. *J. Mater. Chem. A* **2014**, *2*, 19623–19632.
- (26) Jian, Z.; Sun, Y.; Ji, X. A New Low-Voltage Plateau of Na₃V₂(PO₄)₃ as an Anode for Na-Ion Batteries. *Chem. Commun.* **2015**, *51*, 6381–6383.
- (27) Jian, Z.; Zhao, L.; Pan, H.; Hu, Y.-S.; Li, H.; Chen, W.; Chen, L. Carbon Coated Na₃V₂(PO₄)₃ as Novel Electrode Material for Sodium Ion Batteries. *Electrochem. Commun.* **2012**, *14*, 86–89.
- (28) Delacourt, C.; Poizot, P.; Tarascon, J.-M.; Masquelier, C. The Existence of a Temperature-Driven Solid Solution in Li_xFePO₄ for 0 ≤ x ≤ 1. *Nat. Mater.* **2005**, *4*, 254–260.
- (29) Malik, R.; Zhou, F.; Ceder, G. Kinetics of Non-Equilibrium Lithium Incorporation in LiFePO₄. *Nat. Mater.* **2011**, *10*, 587–590.
- (30) Orikasa, Y.; Maeda, T.; Koyama, Y.; Murayama, H.; Fukuda, K.; Tanida, H.; Arai, H.; Matsubara, E.; Uchimoto, Y.; Ogumi, Z. Direct Observation of a Metastable Crystal Phase of Li_xFePO₄ under Electrochemical Phase Transition. *J. Am. Chem. Soc.* **2013**, *135*, 5497–5500.
- (31) Orikasa, Y.; Maeda, T.; Koyama, Y.; Murayama, H.; Fukuda, K.; Tanida, H.; Arai, H.; Matsubara, E.; Uchimoto, Y.; Ogumi, Z. Transient Phase Change in Two Phase Reaction between LiFePO₄ and FePO₄ under Battery Operation. *Chem. Mater.* **2013**, *25*, 1032–1039.
- (32) Owen, J.; Hector, A.; Borkiewicz, O. J.; Wiaderek, K. M.; Chapman, K. W.; Peter, J.; Chupas, C. P. G. Capturing Metastable Structures during High-Rate Cycling of LiFePO₄ Nanoparticle Electrodes. *Science* **2014**, *344*, 1451–1452.
- (33) Nishimura, S.-i.; Natsui, R.; Yamada, A. Superstructure in the Metastable Intermediate-Phase Li_{2/3}FePO₄ Accelerating the Lithium Battery Cathode Reaction. *Angew. Chem., Int. Ed.* **2015**, *54*, 8939–8942.
- (34) Lu, J.; Oyama, G.; Nishimura, S.-i.; Yamada, A. Increased Conductivity in the Metastable Intermediate in Li_xFePO₄ Electrode. *Chem. Mater.* **2016**, *28*, 1101–1106.
- (35) Takahashi, I.; Mori, T.; Yoshinari, T.; Orikasa, Y.; Koyama, Y.; Murayama, H.; Fukuda, K.; Hatano, M.; Arai, H.; Uchimoto, Y.; et al. Irreversible Phase Transition between LiFePO₄ and FePO₄ during High-Rate Charge-Discharge Reaction by Operando X-Ray Diffraction. *J. Power Sources* **2016**, *309*, 122–126.
- (36) Yoshinari, T.; Mori, T.; Otani, K.; Munesada, T.; Yamamoto, K.; Uchiyama, T.; Fukuda, K.; Koyama, Y.; Hagiwara, R.; Orikasa, Y.; et al. Quantitative Elucidation of the Non-Equilibrium Phase Transition in LiFePO₄ via the Intermediate Phase. *Chem. Mater.* **2019**, *31*, 7160–7166.
- (37) Fauth, F.; Peral, I.; Popescu, C.; Knapp, M. The New Material Science Powder Diffraction Beamline at ALBA Synchrotron. *Powder Diffr.* **2013**, *28*, S360–S370.
- (38) Herklotz, M.; Weiß, J.; Ahrens, E.; Yavuz, M.; Mereacre, L.; Kiziltas-Yavuz, N.; Dräger, C.; Ehrenberg, H.; Eckert, J.; Fauth, F.; et al. A Novel High-Throughput Setup for in Situ Powder Diffraction on Coin Cell Batteries. *J. Appl. Crystallogr.* **2016**, *49*, 340–345.
- (39) Kresse, G.; Furthmüller, J. Efficiency of Ab-Initio Total Energy Calculations for Metals and Semiconductors Using a Plane-Wave Basis Set. *Comput. Mater. Sci.* **1996**, *6*, 15–50.
- (40) Vargas-Hernández, R. A. Bayesian Optimization for Calibrating and Selecting Hybrid-Density Functional Models. *J. Phys. Chem. A* **2020**, *124*, 4053–4061.
- (41) Sun, J.; Ruzsinszky, A.; Perdew, J. P. Strongly Constrained and Appropriately Normed Semilocal Density Functional. *Phys. Rev. Lett.* **2015**, *115*, 036402.
- (42) Long, O. Y.; Sai Gautam, G.; Carter, E. A. Evaluating Optimal U for 3d Transition-Metal Oxides within the SCAN+ U Framework. *Phys. Rev. Mater.* **2020**, *4*, 1–15.

- (43) Kresse, G.; Joubert, D. From Ultrasoft Pseudopotentials to the Projector Augmented-Wave Method. *Phys. Rev. B: Condens. Matter Mater. Phys.* **1999**, *59*, 1758–1775.
- (44) Chotard, J.-N.; Rousse, G.; David, R.; Mentré, O.; Courty, M.; Masquelier, C. Discovery of a Sodium-Ordered Form of $\text{Na}_3\text{V}_2(\text{PO}_4)_3$ below Ambient Temperature. *Chem. Mater.* **2015**, *27*, 5982–5987.
- (45) Saurel, D.; Pendashteh, A.; Jáuregui, M.; Reynaud, M.; Fehse, M.; Galceran, M.; Casas-Cabanas, M. Experimental Considerations for Operando Metal-Ion Battery Monitoring Using X-ray Techniques. *Chem. Methods* **2021**, *1*, 249–260.
- (46) Boultif, A.; Louër, D. Powder Pattern Indexing with the Dichotomy Method. *J. Appl. Crystallogr.* **2004**, *37*, 724–731.
- (47) Laugier, J.; Bochu, B. Checkcell. “LMGP-Suite Suite of Programs for the interpretation of X-ray Experiments.” ENSP/Laboratoire des Matériaux et du Génie Physique, BP 46. 38042: Saint Martin d’Hères, France. 2002 <https://lmgp.grenoble-inp.fr/> and <http://ccp14.cryst.bbk.ac.uk/tutorial/lmpg/index.html>.
- (48) Kraus, W.; Nolze, G. POWDER CELL - A Program for the Representation and Manipulation of Crystal Structures and Calculation of the Resulting X-Ray Powder Patterns. *J. Appl. Crystallogr.* **1996**, *29*, 301–303.
- (49) Wang, Z.; Park, S.; Deng, Z.; Carlier, D.; Chotard, J.-N.; Croguennec, L.; Gautam, G. S.; Cheetham, A. K.; Masquelier, C.; Canepa, P. Phase Stability and Sodium-Vacancy Orderings in a NaSICON Electrode. *J. Mater. Chem. A* **2022**, *10*, 309–217.
- (50) Park, S.; Chotard, J.-N.; Carlier, D.; Moog, I.; Courty, M.; Duttine, M.; Fauth, F.; Iadecola, A.; Croguennec, L.; Masquelier, C. Crystal Structures and Local Environments of NASICON-Type $\text{Na}_3\text{FeV}(\text{PO}_4)_3$ and $\text{Na}_4\text{FeV}(\text{PO}_4)_3$ positive Electrode Materials for Na-Ion Batteries. *Chem. Mater.* **2021**, *33*, 5355–5367.
- (51) Lalère, F.; Seznec, V.; Courty, M.; David, R.; Chotard, J. N.; Masquelier, C. Improving the Energy Density of $\text{Na}_3\text{V}_2(\text{PO}_4)_3$ -Based Positive Electrodes through V/Al Substitution. *J. Mater. Chem. A* **2015**, *3*, 16198–16205.
- (52) Wang, J.; Wang, Y.; Seo, D. H.; Shi, T.; Chen, S.; Tian, Y.; Kim, H.; Ceder, G. A High-Energy NASICON-Type Cathode Material for Na-Ion Batteries-Supporting. *Adv. Energy Mater.* **2020**, *10* (). DOI: [10.1002/aenm.201903968](https://doi.org/10.1002/aenm.201903968).
- (53) Lalère, F.; Seznec, V.; Courty, M.; Chotard, J. N.; Masquelier, C. Coupled X-Ray Diffraction and Electrochemical Studies of the Mixed Ti/V-Containing NASICON: $\text{Na}_2\text{TiV}(\text{PO}_4)_3$. *J. Mater. Chem. A* **2018**, *6*, 6654–6659.
- (54) Bianchini, M.; Ateba-Mba, J. M.; Dagault, P.; Bogdan, E.; Carlier, D.; Suard, E.; Masquelier, C.; Croguennec, L. Multiple Phases in the ϵ - VPO_4O - LiVPO_4O - $\text{Li}_2\text{VPO}_4\text{O}$ System: A Combined Solid State Electrochemistry and Diffraction Structural Study. *J. Mater. Chem. A* **2014**, *2*, 10182–10192.
- (55) Masquelier, C.; Wurm, C.; Rodríguez-Carvajal, J.; Gaubicher, J.; Nazar, L. A Powder Neutron Diffraction Investigation of the Two Rhombohedral NASICON Analogues: γ - $\text{Na}_3\text{Fe}_2(\text{PO}_4)_3$ and $\text{Li}_3\text{Fe}_2(\text{PO}_4)_3$. *Chem. Mater.* **2000**, *12*, 525–532.
- (56) Liu, R.; Xu, G.; Li, Q.; Zheng, S.; Zheng, G.; Gong, Z.; Li, Y.; Kruskop, E.; Fu, R.; Chen, Z.; et al. Exploring Highly Reversible 1.5-Electron Reactions ($\text{V}^{3+}/\text{V}^{4+}/\text{V}^{5+}$) in $\text{Na}_3\text{VCr}(\text{PO}_4)_3$ Cathode for Sodium-Ion Batteries. *ACS Appl. Mater. Interfaces* **2017**, *9*, 43632–43639.
- (57) Gaubicher, J.; Wurm, C.; Goward, G.; Masquelier, C.; Nazar, L. Rhombohedral Form of $\text{Li}_3\text{V}_2(\text{PO}_4)_3$ as a Cathode in Li-Ion Batteries. *Chem. Mater.* **2000**, *12*, 3240–3242.

ACS In Focus ebooks are digital publications that help readers of all levels accelerate their fundamental understanding of emerging topics and techniques from across the sciences.



pubs.acs.org/series/Infoxus

ACS Publications

Most Trusted. Most Cited. Most Read.